RSC Advances

PAPER

View Article Online
View Journal | View Issue

Cite this: *RSC Adv.*, 2023, **13**, 35551

Understanding the charge transfer mechanism in $CsPbBr_3$ nanocrystals and nitrogen-doped carbon quantum dot heterostructures: effect of nanocrystal encapsulation†

Smaranika Ray,[a] Mihir Ranjan Sahoo,[b] Susmita Mukherjee,[c] Ajay Perumal,[c] Saroj K. Nayak [b] and Saikat Bhaumik *[ad]

Recently, lead halide perovskite nanocrystal (NC)-based heterostructures have demonstrated significant promise in various research areas, including solar cells, CO_2 reduction, and photocatalysis. These hybrid structures have also played a crucial role in advancing our fundamental conception of charge transfer mechanisms occurring at the interface. A thin shell around the NCs is not suitable for the formation of stable and luminescent materials. However, such NCs are suitable for solar cells, LEDs, CO_2 reduction, and photocatalytic applications due to higher carrier mobility. Thick-shelled NCs are highly stable but hinder charge transport among the NCs which is beneficial for bio-imaging and color-converted LED fabrication. So, understanding the mechanism of charge transport among the NCs dependent on the shell materials is important. Here, we synthesized $CsPbBr_3$ NCs with various coating materials to vary the effective distance between the perovskite and nitrogen-doped carbon quantum dots (NCQDs) to understand the charge transfer process among them. We encapsulated the NCs with different coating materials (*i.e.*, oleic acid, oleylamine, polyvinylpyrrolidone, and silica) such that the thickness of the NCs' shell can differ. We observed that the charge transfer rate between thick-shelled NCs and NCQDs is slow. The faster charge transfer among the thinner-shelled NCs and NCQDs is feasible due to the bonding of the N-state of NCQDs with Pb-atoms of the $CsPbBr_3$ structure. The density functional theory (DFT) calculations of the heterostructure indicate that the electron acceptor state of the N-atom in NCQDs lies below the conduction band of perovskite NCs, which is accountable for such charge transfer. This study has immense significance as it provides crucial insights into the design and application of heterostructures, which can be extended to various novel opportunities for progress and innovation.

Received 15th September 2023
Accepted 1st December 2023

DOI: 10.1039/d3ra06307k

rsc.li/rsc-advances

Introduction

Recently, all inorganic $CsPbX_3$ (X = I, Br, Cl) perovskite nanocrystals (NCs) have evolved as promising materials that express great potential in numerous optoelectronic applications, such as LEDs, photovoltaics, photodetectors, lasers, sensors, *etc.* The perovskite NCs exhibit some fascinating properties, like huge absorption coefficient, feasible bandgap tunability, high photoluminescence quantum yield (PLQY), narrow emission full-width half maxima (FWHM), favorable carrier mobility, and easier solution processability.[1–7] The color tunability of the NCs can be achieved by adjusting the size, shape, composition, and crystallinity of the NCs. $CsPbBr_3$ NCs are typically crystallized into cubic, orthorhombic, or monoclinic perovskite structures.[8–10] Among them, cubic and orthorhombic structures remained stable at high temperatures (>130 °C), while the monoclinic structure is stable at room temperature. The $CsPbBr_3$ NCs are usually synthesized by either hot injection or ligand-assisted re-precipitation (LARP) synthesis methods.[11,12] The hot-injection process requires an inert atmosphere, a comparatively higher reaction temperature (>150 °C), and it is a time-consuming process. On the other hand, the synthesis of the NCs can be achieved *via* the room-temperature LARP synthesis technique under an open atmosphere, which facilitates the growth of different sizes and shapes of NCs.[12,13]

[a]*Department of Engineering and Materials Physics, Institute of Chemical Technology-IndianOil Odisha Campus, Bhubaneswar, Odisha, India, 751013*

[b]*School of Basic Sciences, Indian Institute of Technology Bhubaneswar, Khordha, Odisha, India, 752050*

[c]*Functional NANO and Opto-electronics Lab (FNOL), Department of Physical Sciences, Indian Institute of Science Education and Research (IISER), Berhampur, Odisha, India, 760010*

[d]*Department of Physics, Indian Institute of Technology Guwahati, Assam, India, 781039. E-mail: s.bhaumik@iitg.ac.in*

† Electronic supplementary information (ESI) available. See DOI: https://doi.org/10.1039/d3ra06307k

Besides their unique features, poor structural stability of the perovskite materials against air, moisture, and heat impedes practical implementation in real-world applications. Perovskite materials degrade due to their inherent ionic nature and encapsulation of the surface atoms with loosely bound dynamic organic ligands [*i.e.*, oleic acid (OA) and oleylamine (OAm)].[14,15] Many efforts have been implemented to improve the NCs' stability and emission intensity. Bhaumik *et al.* synthesized $MAPbBr_3$ core and high bandgap octylammonium lead bromide [$(OCA)_2PbBr_4$] shell for the formation of core@shell type NCs *via* LARP synthesis technique that showed better structural stability and emission intensity.[16] Doping with different metal ions (*e.g.*, Zn, Mg, Rb, *etc.*) inside the perovskite structure and also encapsulation of the NCs with various stable coating materials (*e.g.*, metal oxides, metal chalcogenides, polymers, metal–organic frameworks, *etc.*) were found to be some of the effective ways to improve the NCs' stability and photoluminescence (PL) intensity.[17–21] Double-coated NCs exhibit superior emission properties and better stabilities which are suitable for various applications.[22–24]

Heterostructure materials play a crucial part in the development of semiconducting industry. The combination of different semiconducting materials with variable band positions resulting in the formation of suitable heterostructures that enable formation of various optoelectronic devices and photocatalytic applications.[25–27] The charge carriers can be confined within specific regions of the heterostructures by manipulating the energy levels of the semiconductors. Many devices, such as solar cells, photodetectors, and transistors were fabricated from heterostructure materials, where band alignment at the interfaces plays a significant role. Recently, several heterostructures were synthesized among $CsPbBr_3$ NCs and different metal chalcogenide semiconductors (ZnS, CdS, PbS, *etc.*) which possess either type-I or type-II band alignments.[28–31] Such heterostructures demonstrate excellent emission and carrier transport properties. Heterostructures made of $CsPbBr_3$ NCs and 2D structured materials (*e.g.*, graphene oxide, MXene, MoS_2, *etc.*) exhibit efficient optoelectronic properties, higher photoresponse, and excellent CO_2 reduction capability.[32–35]

However, the properties of $CsPbBr_3$ NCs and carbon quantum dots (CQDs) heterostructure system of were not much explored. The optical properties of CQDs can be tuned by nitrogen doping which forms electron acceptor states below the conduction band.[36] Such electron acceptor states in nitrogen-doped carbon quantum dots (NCQDs) facilitate the charge separation in the heterostructure. The dependency of NCs' shell thickness and the bonding between the two materials that are responsible for such charge separation are not explored. In this regard, we studied the charge transfer mechanism of a heterostructure formed by mixing Zn-doped $CsPbBr_3$ NCs and NCQDs. We synthesized Zn-doped $CsPbBr_3$ NCs *via* LARP synthesis method and NCQDs were prepared by hydrothermal method. We observed that the PL quenching of the perovskite NCs due to the heterostructure formation with NCQDs. We explored the dependency of charge transfer rate among them with a varying shell thickness around the Zn-doped $CsPbBr_3$ NCs. We carried out time-resolved PL spectroscopy (TRPL) and density functional theory (DFT) studies to understand the PL quenching mechanism in the heterostructure system. Additionally, we have investigated the more robust bond formation between the surface of $CsPbBr_3$ and NCQDs, which leads to charge transfer inside the heterostructure.

Experimental section

Materials required

CsBr (99.99% trace metals basis), $PbBr_2$ (99.99% trace metals basis), $ZnBr_2$ (99.9%, trace metal basis), citric acid monohydrate (CA, ACS reagent, ≥99.0%), *o*-phenylenediamine (*o*-PDA, 99.5%), *N*,*N*′-dimethylformamide (DMF, anhydrous, 99.8%), (3-aminopropyl)trimethoxysilane (APTMS, 97%), poly(-vinylpyrrolidone) (PVP, avg. M_n ~40 000), OA (90%), OAm (70%), toluene (anhydrous, 99.8%), and acetonitrile (ACN, 99.95%) were purchased from Sigma Aldrich company. *n*-Octylammonium bromide (OCABr, 99%) was purchased from Greatcell Solar Materials company. Ethanol (absolute for analysis, 99%) was purchased from Merck company. All chemicals were used without further purification.

Synthesis of OA–OAm capped Zn-doped $CsPbBr_3$ NCs

OA–OAm capped Zn-doped $CsPbBr_3$ NCs were synthesized by the modified LARP method under normal atmospheric conditions.[16] At first, four precursor solutions were prepared in separate glass vials by dissolving 0.16 mmol CsBr, 0.16 mmol $PbBr_2$, 0.16 mmol $ZnBr_2$, and 0.16 mmol of OCABr in 2 mL of DMF. The precursor solutions were mixed properly *via* vigorous stirring to complete the dissolution of the salts. Then, the final precursor was attained by mixing 800 μL of CsBr precursor, 200 μL of OCABr precursor, 1 mL of $PbBr_2$ precursor, 400 μL of $ZnBr_2$ precursor, 100 μL of OAm, and 200 μL of OA in a separate glass vial. Finally, 1 mL of the final precursor solution was swiftly injected into a round bottom flask containing 20 mL of toluene. The nucleation was continued for 15 min and then the solution was transferred to a centrifuge tube. 4 mL of ACN was added to the NCs solution and then centrifuged at 6000 rpm for 10 min. The supernatant was discarded and precipitation of the NCs was redispersed in toluene for further characterization. The purified NCs are renamed CPB@OA NCs.

PVP encapsulation around CPB@OA NCs

PVP-coated Zn-doped $CsPbBr_3$ NCs were synthesized by the modified LARP method under room temperature.[37] The final precursor was arranged by following the previous CPB@OA NCs synthesis process. Finally, the PVP solution (20 mg PVP dissolved in 500 μL of ethanol) was added to 20 mL of toluene in a round bottom flask. Then, 1 mL of the final precursor was injected dropwise into the flask under vigorous stirring conditions and continued for 15 min. Later, 4 mL of ACN was added to the NCs solution contained in a centrifuge tube and centrifuged at 6000 rpm for 10 min. Finally, the precipitate can be redispersed in toluene for further characterization. The NCs are renamed as CPB@OA@PVP NCs.

Synthesis of silica-coated Zn-doped $CsPbBr_3$ NCs

Silica-coated Zn-doped $CsPbBr_3$ NCs were synthesized by the modified LARP method under normal atmospheric conditions.[38] The final precursor CsBr, OCABr, $PbBr_2$, and $ZnBr_2$ precursors were added in the same ratios to make a clear transparent precursor solution. Finally, 20 μL of APTMS was mixed with a transparent precursor solution to form a final precursor solution. Then 1 mL of the final precursor was swiftly injected dropwise in a round bottom flask containing 20 mL of toluene under vigorous stirring. After injection, the stirring speed was slowed down to complete the hydrolysis of APTMS into SiO_2. The NCs solution was centrifuged at 3000 rpm for 10 min. The supernatant was discarded, and the precipitate was dispersed in ethanol for further characterization. The silica-coated NCs are renamed CPB@SiO NCs.

Post-treatment of CPB@SiO NCs with PVP

Post-synthetic PVP treatment was carried out by adding synthesized CPB@SiO NCs with PVP polymer under normal atmospheric conditions. For this process, 4 mL of CPB@SiO NCs (concentration ~10 mg mL^{-1}) was added into 20 mg PVP polymer in a round bottom flask and continued stirring for 5 hours.[22] Later, the NCs solution was centrifuged at 3000 rpm for 10 min. Then the precipitate was collected and dispersed in ethanol for further characterization. The PVP polymer was adsorbed into the SiO_2 surface and they are renamed as CPB@SiO@PVP NCs.

Synthesis of NCQDs

NCQDs were prepared by hydrothermal method using CA as carbon and *o*-PDA as a nitrogen source, respectively.[39] First, CA (0.420 g, 2 mmol) and *o*-PDA (0.432 g, 4 mmol) were dissolved and sonicated in 20 mL of DI water. The clear transparent solution was transferred into a 25 mL Teflon-lined autoclave and heated at 160 °C for 8 hours. The autoclave was naturally cooled to room temperature after the reaction. A brown aqueous crude solution was formed that was centrifuged at 6000 rpm for 20 min and filtered using a 0.22 μm membrane filter to remove agglomerated particles. Finally, the solution was evaporated by a rotary evaporator, and the precipitate was collected and redispersed in ethanol for further characterization.

Computational details

The Vienna *ab inito* simulation package (VASP) code based on plane wave density functional theory (DFT) was used to calculate the structural and electronic properties of NCQDs adsorbed on the $CsPbBr_3$ surface.[40,41] In this work, the exchange-correlation function was approximated with the Perdew–Burke–Ernzerhof (PBE) version of generalized gradient approximation (GGA).[42] A kinetic energy cut-off of 500 eV was used to describe the plane wave basis set. A *k*-point grid of $3 \times 3 \times 1$ was chosen for self-consistent calculations for the system containing $CsPbBr_3$ slab, whereas a higher *k*-point grid of $7 \times 7 \times 1$ was considered for the analysis of the density of states (DOS).[43] Using Grimme's DFT-D2 method, the van der Waals correction was included. The threshold for energy convergence between two consecutive steps was set to 1×10^{-4} eV and the structures were optimized until the force on each atom became less than 0.02 eV $Å^{-1}$. A large vacuum space of 20 Å was taken along the *z*-direction to prevent interactions between periodic images.

Results and discussion

The UV-VIS absorption and PL spectroscopies of the NCs were conducted in solution phase and corresponding spectra are shown in Fig. 1a. The absorption spectra of CPB@OA and CPB@OA@PVP NCs (dispersed in toluene) reveal a nearly identical pattern with an absorption peak position at around 513 nm. The bandgap value of these NCs is 2.24 and 2.27 eV, as calculated from the Tauc plots (see Fig. S1a and b in ESI†). These NCs also exhibit a similar PL spectrum with an emission peak position at around 516 nm (FWHM ~22 nm). The measured PLQY was around 56% for CPB@OA NCs and 68% for CPB@OA@PVP NCs. The low emission intensity of OA and OAm-capped CPB@OA NCs is attributed to the dynamic characteristics of the capping ligands that do not adequately passivate the surface of the NCs and causes the formation of surface trap states.[15,44,45] These trap states impede the radiative recombination of the excitons, leading to reduced emission intensity. However, PVP coating around the CPB@OA NCs (*i.e.*, CPB@OA@PVP NCs) reduces the surface dangling bonds and results in improved emission intensity.[37,44] The absorption spectrum of the CPB@SiO NCs reveals an absorption peak position at 506 nm. The bandgap value of the NCs is to be 2.26 eV as calculated from the Tauc plot (see Fig. S1c in ESI†). The PL emission peak position of the NCs is located at 511 nm (FWHM ~25 nm) with a PLQY of 80%. The effective surface passivation of the NCs with silica reduces defect states in the surface and promotes excitonic radiative recombination.[22,38,46] The CPB@SiO@PVP NCs show an absorption peak position at

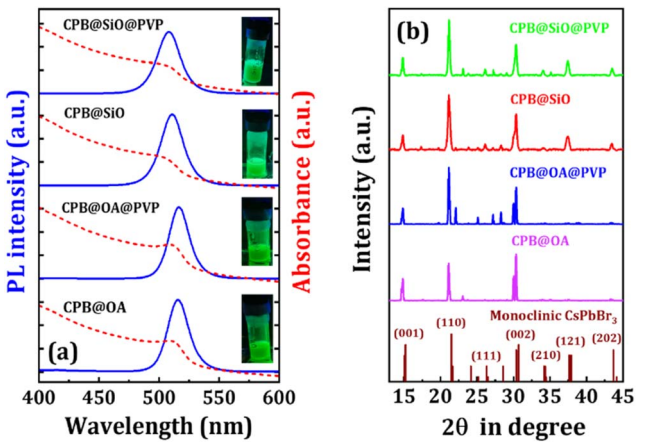

Fig. 1 (a) UV-VIS absorption (dotted red lines) and PL (solid blue lines) spectra of different NCs as marked in the figure. (Inset) photographic image of all NCs solutions under a UV lamp. (b) XRD diffraction patterns of different NCs as marked in the figure. The bottom of the figure represents the standard diffraction pattern of the monoclinic $CsPbBr_3$ crystal structure.

505 nm and PL emission peak at 508 nm (PLQY ~84%). The PVP passivation around the CPB@SiO NCs (*i.e.*, CPB@SiO@PVP NCs) leads to a minor blue shift in the PL emission spectrum, potentially indicating the quantum confinement effect on the charge carriers inside the NCs.

The X-ray diffraction (XRD) measurement of the NCs were performed in the thin film form for analyzing the phase purity and the diffraction patterns are represented in Fig. 1b. The XRD diffraction patterns of all the NCs match quite well with the standard diffraction spectrum of the monoclinic $CsPbBr_3$ phase (JCPDS #00-18-0364). The diffraction peaks at the angles of 14.8°, 21.1°, 26.1°, 30.3°, 34.0° for all NCs, correspond to the (001), (110), (111), (002), (210) lattice planes of the monoclinic perovskite phase.[10,22] Additional peaks at 37.3°, and 43.5° are also visible for both silica-coated NCs (*i.e.*, CPB@SiO and CPB@SiO@PVP NCs) from (121) and (202) lattice planes of same monoclinic phase. A slight shift in XRD peaks towards a lower angle is noticed as compared to standard diffraction pattern of monoclinic $CsPbBr_3$ phase, which can be attributed due to the contraction of the perovskite crystal structure while substituting Pb lattice sites with comparatively smaller Zn-ions in the perovskite structure.[23,47] For the confirmation of the presence of Zn-ions in $CsPbBr_3$ NCs, we conducted X-ray Photoelectron Spectroscopy (XPS) measurement. The full XPS spectrum shows the presence of Zn 2p, Br 3d, Pb 4f, and Cs 3d chemical states as represented in Fig. S2a.†[38] The XPS peaks appeared at 1022.47 eV ($2p_{1/2}$ state) and 1045.6 eV ($2p_{3/2}$ state) confirming the presence of Zn-ions in the $CsPbBr_3$ crystal lattice (see Fig. S2b†).

The transmission electron microscopy (TEM) images of the CPB@OA and CPB@OA@PVP NCs are represented in Fig. 2a and b, respectively. The images reveal a cubical shape of the NCs. The CPB@OA NCs have slightly irregular bigger particle size distributions due to the tendency of agglomeration among the other NCs.[48–50] However, the PVP coating on CPB@OA NCs reduces the agglomeration effect and maintains uniform and well spreads particles.[51] The average edge size of the NCs is distributed within the range of 10–20 nm. The inter-planner spacing of both these NCs was measured from the corresponding HRTEM images (inset of Fig. 2a and b). The calculated lattice spacing is calculated to be ~0.43 nm, corresponding to the (110) lattice plane of the monoclinic $CsPbBr_3$ crystal structure.[51] The TEM image of CPB@SiO NCs (see Fig. 2c) shows asymmetrical particle sizes because the silica shells diffuse among themselves and transform into bigger NCs. The slightly blurred surface of thickness 3–5 nm around the NCs appears from the growth of compact silica shelling.[23,52] The encapsulation of PVP around silica-coated NCs (*i.e.*, CPB@SiO@PVP NCs) slightly prevents the NCs agglomeration. The CPB@SiO and CPB@SiO@PVP NCs exhibit similar inter-planar spacing of ~0.6 nm, which resembles (100) lattice planes of monoclinic $CsPbBr_3$ phase (inset of Fig. 2c and d).[38]

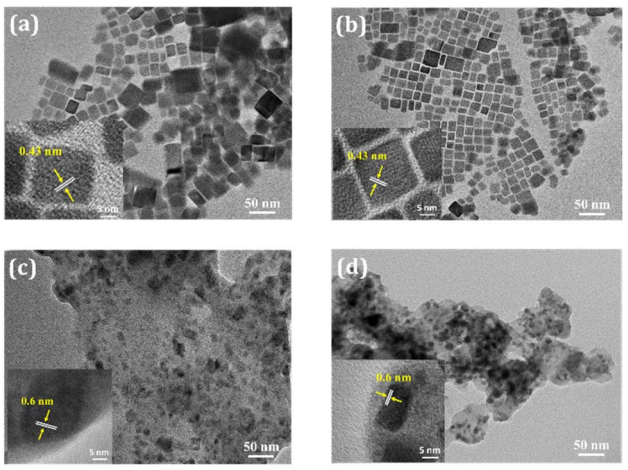

Fig. 2 TEM images of (a) CPB@OA, (b) CPB@OA@PVP, (c) CPB@SiO, and (d) CPB@SiO@PVP NCs. Insets: HRTEM images of respective NCs.

Fourier transform infrared (FTIR) of the NCs was performed to understand the attachment of different shelling materials around the NCs surface. The spectra of the NCs are represented in Fig. S3 (in ESI†). The FTIR spectrum of CPB@OA NCs reveals different peaks located at 1492 and 3033 cm^{-1} that are corresponding to –COO and –OH functional groups in OA capping ligands, respectively.[15] An additional peak located at 723 cm^{-1} originates from CH deformation of *cis*-disubstituted alkenes of OAm capping ligands. These results suggest the presence of OA and OAm capping ligands around both CPB@OA and CPB@OA@PVP NCs. Along with these peaks, some additional peaks are noticed at 1458, 1609, and 3039 cm^{-1} in CPB@OA@PVP NCs that invent from C–H, C=O stretching vibrations, and asymmetric CH_2 groups present in the PVP polymer.[53,54] The peaks present at 1066 and 867 cm^{-1} in CPB@SiO NCs are attributed to the asymmetric stretching of the Si–O–Si bonds and symmetrical stretching vibrations of the Si–O bonds, respectively which reveals the hydrolysis of silica around the $CsPbBr_3$ NCs.[52,55] The FTIR spectrum of CPB@SiO@PVP NCs exhibits similar peaks as observed for CPB@SiO NCs. However, an additional absorption peak appeared at 1451 cm^{-1} that conforming the C–H bending vibrations of PVP polymer.[53]

The UV-VIS and PL spectra of NCQDs are demonstrated in Fig. 3a. The UV-VIS spectrum of NCQDs shows strong absorption peaks at 310 and 378 nm attributed to n–π* transitions, suggesting the absorption by surface groups containing nitrogen or oxygen in the NCQDs.[56] Two characteristic peaks 272 and 278 nm are also appeared which ascribed to the π–π* transitions of C=C and C=N bonds, respectively.[57,58] The PL spectrum of NCQDs reveals a wide-ranging emission spectrum centered at 460 nm (FWHM ~100 nm). The NCQDs solutions appeared colorless under the sunlight and emitted blue fluorescence while placed under a UV lamp (see inset of Fig. 3a). The NCQDs retain their PL intensity for up to six months while dispersed in ethanol, demonstrating excellent chemical and optical stability. The XRD diffraction pattern of NCQDs film displays a broad diffraction peak centered at around 23° (see Fig. 3b), representing the characteristics diffraction pattern of amorphous carbon. The FTIR spectrum of NCQDs is shown in Fig. 3c. Two vibrational peaks appeared at 3685 and 3668 cm^{-1} arising from O–H and N–H stretching, respectively. A broad peak originating in the range of 2989–2895 cm^{-1} is ascribed to

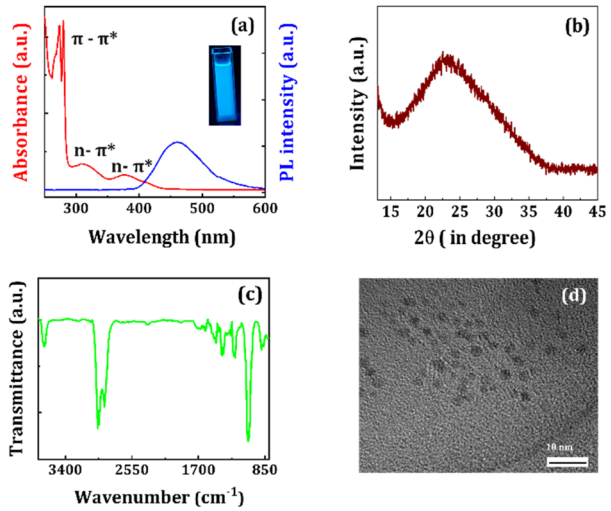

Fig. 3 (a) UV-VIS absorption (red line) and PL (blue line) spectra of NCQDs. Inset: photographic image of NCQDs in ethanol while placed under a UV lamp. (b) XRD diffraction pattern, (c) FTIR spectrum, and (d) TEM image of NCQDs.

the C–H saturated hydrocarbons. The additional peaks located at 1474, 1397, and 1231 cm^{-1} are attributed due to C=O, C–N, and C–O stretching vibrations of NCQDs, respectively.[59,60] The TEM image reveals the spherical shape of NCQDs having a nearly uniform particle size distribution in the range of 3–5 nm (see Fig. 3d). The presence of N-atoms in NCQDs is identified from FESEM-EDS mapping as depicted in Fig. S4 (see ESI†). The atomic weight percentage was calculated to be around 58.33% for C-atoms, 12.99% for N-atoms, and 28.68% for O-atoms for the NCQDs film.

We took each perovskite NCs solution in 2 mL solvent such that the absorbance peak value of the NCs was maintained at 0.1. Then we added different volumes of NCQDs solution (conc. ~7 mg mL^{-1}) in the respective perovskite NCs solutions and recorded the UV-VIS absorption (see Fig. 4) and PL spectra (see Fig. 5a–d) of the mixture. The absorption peak positions of both CPB@OA and CPB@OA@PVP NCs are located at around 510 nm. There are no significant changes in the peak positions of the NCs are observed after addition of NCQDs in the respective NCs solutions. However, significant enhancements in absorbance value in the range of 300–400 nm are noticed, corresponding to characteristic peaks of NCQDs. With increasing the volume of NCQDs in the mixture, the absorbance of NCQDs also rises proportionately, but there is no change in absorption spectrum of perovskite NCs. Similar characteristics were also observed when NCQDs were mixed with CPB@SiO and CPB@SiO@PVP NCs. These results suggest that the NCQDs do not degrade the perovskite crystal structure. We also noticed that the addition of NCQDs in perovskite NCs resulted in a reduction in the PL intensity of the NCs. Among them, the PL intensity of OA–OAm capped NCs decreases faster as compared to silica-coated NCs. The comparison plot of all NCs' PL intensity *versus* NCQDs concentration is shown in Fig. 5e. The Fig. 5f represents the photographic images of all NCs solutions placed under a UV lamp with and without NCQDs. It can also be seen that by increasing the volume of NCQDs, the PL intensity of the perovskite NCs quenches proportionately. With the incorporation of 25 μL of NCQDs, the PL intensities of CPB@OA,

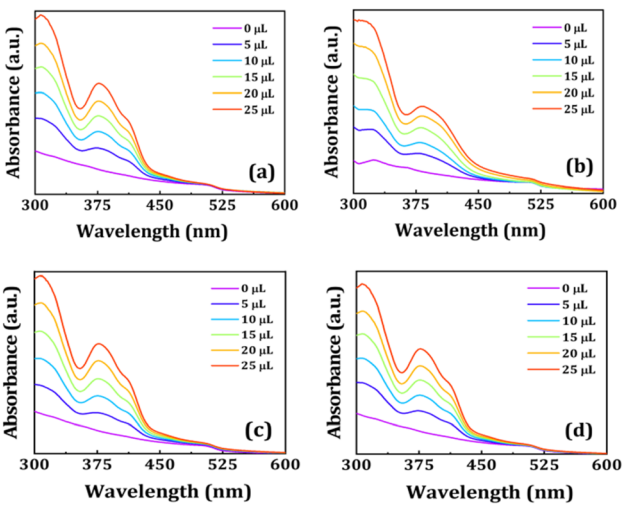

Fig. 4 Variation in UV-VIS spectra of (a) CPB@OA, (b) CPB@OA@PVP, (c) CPB@SiO, and (d) CPB@SiO@PVP NCs, after addition of different volumes of NCQDs, as shown in legends.

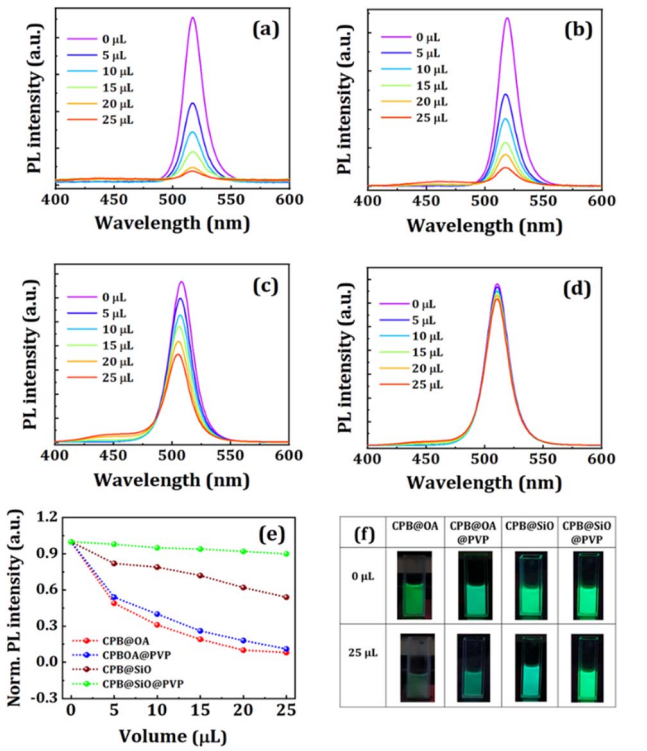

Fig. 5 Change in PL intensity of (a) CPB@OA, (b) CPB@OA@PVP, (c) CPB@SiO, and (d) CPB@SiO@PVP NCs with addition of different volumes of NCQDs as shown in legends. (e) The decrease in PL intensity of all NCs over different volumes of NCQDs as shown in legend. (f) Photographic images of different perovskite NCs under a UV lamp before and after addition of NCQDs in the respective NCs solutions.

CPB@OA@PVP, CPB@SiO, and CPB@SiO@PVP NCs are retained as about 9%, 11%, 54%, and 90% of their respective original PL intensity values, respectively.

To further understand the charge carrier recombination dynamics, we performed time-correlated single-photon counting (TCSPC) of the bare NCs and heterostructures (see Fig. 6a–d). The fitting parameters of the PL decay plots for all NCs are represented in Tables S1–S4 in ESI.† The τ_1 value is associated with trap-assisted recombination involving defects, whereas τ_2 value is attributed to excitonic radiative recombination of NCs, as shown in Fig. S5 (in ESI†).[6,61,62] The trap states originate from halide vacancies present at Pb interstitials and outmost surface of the NCs. The lesser number of defect states leads to lower non-radiative recombination depicting a higher excited lifetime of excitons. The lifetime decay of charge carriers for different NCs with the addition of NCQDs is shown in Fig. 6e. The average PL decay lifetime of OA–OAm capped $CsPbBr_3$ NCs is comparatively small (6.21 ns). It can be noticed that the decay lifetime value increases with PVP shelling around the NCs, which signifies the effective surface passivation of the NCs and increases radiative recombination. The PL decay lifetime of silica-coated $CsPbBr_3$ is 13.29 ns which is longer than OA–OAm capped NCs, implying the dense silica coating around the NCs. The decay lifetime of the NCs further increases with PVP coating. The average PL lifetime of CPB@OA NCs decreases from 6.21 to 1.33 ns with the addition of 25 μL of NCQDs. Similarly, the average lifetime of CPB@OA@PVP, CPB@SiO, and CPB@SiO@PVP NCs changes from 7.51 to 2.69 ns, 13.29 to 9.82 ns, and 16.17 to 15.09 ns after the addition of the same volume of NCQDs solutions, respectively. With increasing the adequate shell thickness around the $CsPbBr_3$ NCs the rate of PL quenching and decay in the PL lifetime are reduced. These results indicate that the interaction of NCQDs with the perovskite NCs is lower if the effective shell thickness of the NCs increases. Table 1 represents the average PL decay lifetime values of all the NCs solutions before and after the addition of different volume of NCQDs.

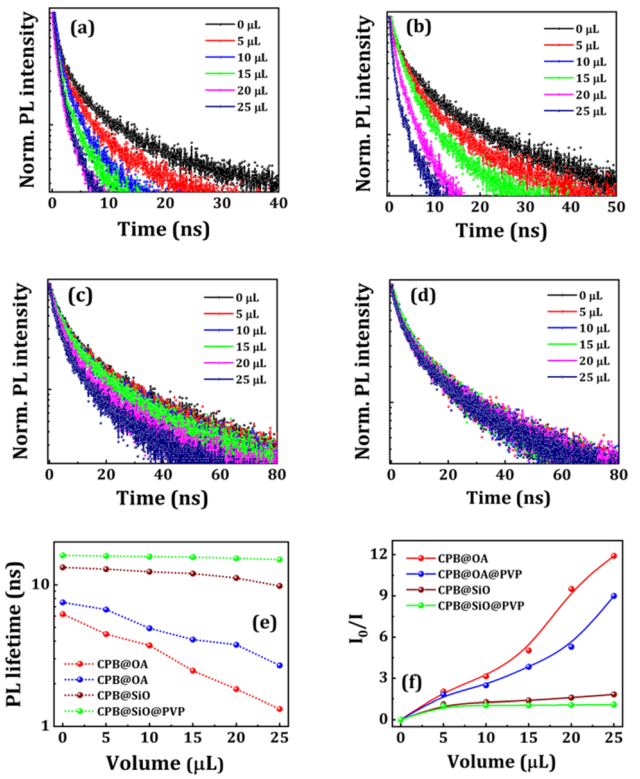

Fig. 6 TRPL decay spectra of (a) CPB@OA, (b) CPB@OA@PVP, (c) CPB@SiO, and (d) CPB@SiO@PVP NCs before and after addition of different volumes of NCQDs, as shown in legends. (e) The decrease in PL lifetime, and (f) Stern–Volmer plot of these NCs over addition of different volumes of NCQDs, as shown in legends.

We observed a reduction in the PL intensity of NCs with the addition of different volumes of NCQDs. The PL quenching is generally attributed due to various factors, which includes degradation of material, energy transfer, or charge transfer processes. To confirm the fact, we have performed XRD analysis of the NCQDs and perovskite NCs mixture films (see Fig. S6 in ESI†). The XRD pattern resembles the monoclinic $CsPbBr_3$ crystal structure. However, a broad peak around 22–23° are appeared from the amorphous NCQDs. There is no observable change in the XRD peak intensity of all NCs when NCQDs were introduced. It shows that there is no lattice deformation or degradation occurred by the addition of NCQDs in perovskite NCs. So, either energy transfer or charge transfer processes are responsible for such PL quenching. Since there is no spectral overlap between absorption spectrum of NCQDs and emission spectrum of NCs, the energy transfer or FRET-induced PL quenching mechanism can be ignored (see Fig. S7 in ESI†).[63,64] Thus, charge transfer is the most feasible mechanism involved in such heterostructures.[36]

The charge transfer process represents the relocation of electrons from one material to another while keeping a small distance between the donor and acceptor materials.[65,66] To

Table 1 Lifetime data of all NCs before and after the addition of different volumes of NCQDs solutions

	Average PL decay lifetime (ns)			
Vol. of NCQDs (μL)	CPB@OA	CPB@OA@PVP	CPB@SiO	CPB@SiO@PVP
0	6.21	7.51	13.29	16.17
5	4.48	6.69	12.92	16.01
10	3.73	4.93	12.39	15.85
15	2.47	4.10	12.01	15.70
20	1.83	3.77	11.19	15.42
25	1.33	2.69	9.82	15.09

understand the mechanism of charge transfer we have performed Stern–Volmer analysis by using the Stern–Volmer equation,

$$I_0/I = \tau_0/\tau = (1 + K[Q])$$

here I_0 and I denote the PL intensities of $CsPbBr_3$ NCs before and after addition of NCQDs, K is the quenching constant and [Q] is the concentration of NCQDs. Fig. 6f represents the Stern–Volmer plot for PL quenching in the presence of various concentrations of NCQDs. The upward curvature in CPB@OA and CPB@OA@PVP NCs indicates that the PL quenching process is not solely governed by a simple collision between NCs and NCQDs, additional factors such as static and dynamic quenching mechanisms also influence the quenching process.[36,64,67] The enhancement of the absorption value of NCQDs with increasing the NCQDs concentration, suggests the possibility of ground-state complex formation in the heterostructure relates to static quenching.[67] The reduction of PL intensity and decay lifetime of such heterostructures suggest the emission decay process involves dynamic quenching.

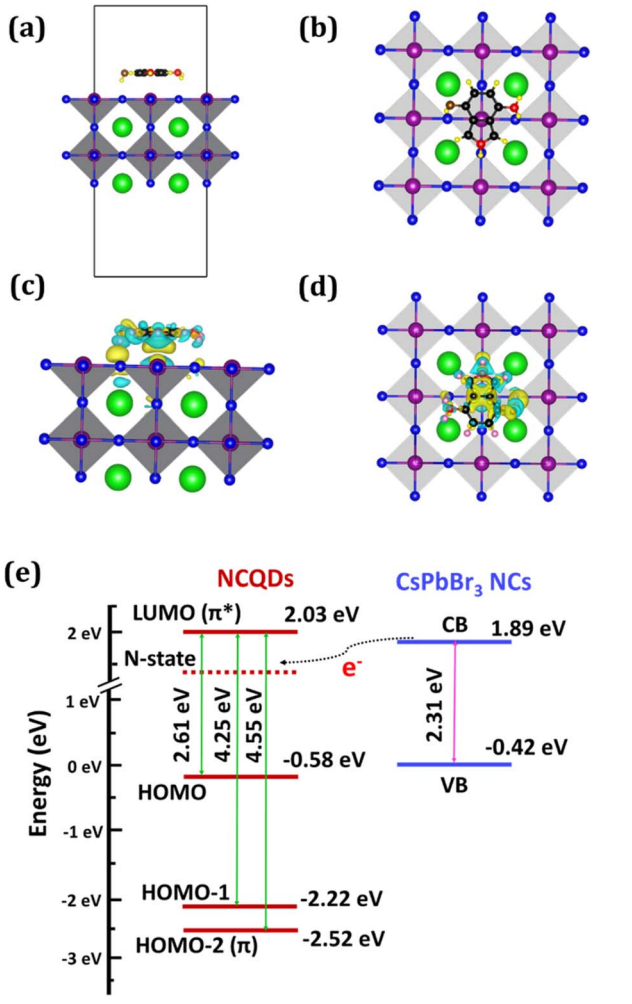

Fig. 7 Schematic diagrams of (a) side and (b) top views of NCQDs adsorbed on $CsPbBr_3$ surface, (c) and (d) represent the schematic side and top views of the charge density differences (iso-surface = 0.001 e $Å^{-3}$). Electron accumulation and depletion regions are represented by yellow and cyan colors respectively (Cs: green, Pb: magenta, Br: blue, C: black, N: red, and H: yellow). (e) Schematic energy band diagrams of $CsPbBr_3$ NCs and NCQDs, showing the route of electron transfer from the CB of $CsPbBr_3$ to the N-state of NCQDs.

The decrease in PL intensity of the $CsPbBr_3$ NCs in presence of NCQDs occurs due to the charge transfer of electrons from the conduction band of NCs to some specific energy states of NCQDs. We calculated the band structure alignment of the heterostructure and possible charge transfer process from the DFT studies to understand the process. Here we considered the simple cubic phase of $CsPbBr_3$ structure ($Pm3m$, 221) for perovskite NCs in our theoretical calculations. In the unit cell, the Pb atom lies in the center, surrounded by six Br atoms to form an octahedron and Cs atom lies at each cubic corner. The lattice constant after the relaxation was found to be 6.01 Å which is in good agreement with previous theoretical and experimental reports.[68,69] Based on the calculated lattice parameter of the optimized bulk structure of cubic $CsPbBr_3$, the slab model of (100) surface of $CsPbBr_3$ was designed to study the adsorption of NCQDs. A four-atomic layer supercell with two PbBr layers and two CsBr layers was chosen where structure of NCQDs was positioned above the PbBr-terminated surface (see Fig. 7a and b). The size of the supercell consisting of $CsPbBr_3$ slab and NCQD molecule was taken as 12.03 Å × 12.03 Å along XY direction which can provide enough space to avoid the lateral interaction between images of NCQDs created due to periodicity involved in the calculation. We intended the charge density difference of NCQDs (see Fig. 7c and d) in the most stable adsorption configuration on $CsPbBr_3$ (001) lattice plane from the formula,

$$\Delta\rho(r) = \rho_{(\text{surface+NCQDs})} - \rho_{\text{surface}} - \rho_{\text{NCQDs}}$$

It is found that electrons are primarily accumulated in the region between NCQDs and the surface. A charge depletion region is observed on the top of the Pb atoms and lies below to NCQDs, indicating the charge transfer from the Pb atoms. On the other hand, the Br atoms gain some negative charge which is clear from the large charge accumulation region. The more accumulation density indicates a stronger bond between the adsorbent and the surface. We performed Bader charge analysis to quantitatively analyze the charge transfer between $CsPbBr_3$ and NCQDs. In the heterostructure, the charge on doped N-atom of NCQDs is $-1.19e$, whereas the charges on N- and O-atoms of the NH_2 and OH functional groups are $-1.29e$ and $-1.24e$, respectively. A very negligible charge of $0.026e$ is transferred from the whole NCQDs to Pb–Br terminated $CsPbBr_3$ surface after the adsorption of NCQDs on $CsPbBr_3$ (001) lattice planes. The band energy levels of the heterostructure are depicted in Fig. 7e. It shows the electron transfer route from conduction band (CB) of $CsPbBr_3$ NCs to the N-state of NCQDs.

To visualize the effect of the adsorption of NCQDs on the electronic structure of $CsPbBr_3$, we plotted the projected band structures and projected DOS (PDOS) of both pristine and NCQDs adsorbed $CsPbBr_3$ surfaces as shown in Fig. 8. The

bandgap of the pristine $CsPbBr_3$ (100) surface was calculated to be 2.31 eV which represents a direct bandgap material (see Fig. 8a). Here, the valence band maximum (VBM) and conduction band minimum (CBM) both lie at −0.42 eV and 1.89 eV, respectively, at the gamma point. While the positions of HOMO levels are −2.52 eV (π), −2.22 eV and −0.58 eV and LUMO level is present at 2.03 eV (π*) for NCQDs. When NCQDs are adsorbed on the $CsPbBr_3$ surface, the bandgap is drastically reduced and found to be 0.92 eV which is clear from Fig. 8b. The combined contributions of 2p orbitals of N and C atoms are found in the extra energy level present below the Fermi level at −0.53 eV. NCQDs produce an acceptor state below the CBM of $CsPbBr_3$, creating a quasi-type II band alignment with the $CsPbBr_3$ slab.[36] This effect can only be observed when NCQDs are adsorbed on the $CsPbBr_3$ slab. To support it, we also calculated the projected band structure of NH_3 molecule adsorbed on the perovskite slab, where no states from NH_3 in the bandgap regime of the slab are observed (see Fig. S8 in ESI†). Thus, the bandgap of the adsorbed slab remains almost like the pristine one. In addition, the valence bands of the $CsPbBr_3$ slab are pushed away from the Fermi level indicating the electrons are transferred between the slab and NCQDs. To get more insight into the interaction between the orbitals of the constituent atoms, we calculated PDOS of both systems as shown in Fig. 8c and d. In the deeper valence band region of the $CsPbBr_3$ slab, an overlap between 5p of Cs-atom and 6s of Pb-atom is observed. The states in the valence band region are dominated mainly by 4p orbital of Br-atom ranging from −4 to 0 eV. In addition, the hybridization of 6s and 6p orbitals of Pb-atom with 4p of Br-atom just below the Fermi level is responsible for the formation of the VBM of the slab. On the other hand, the CBM of $CsPbBr_3$ is formed due to the significant contribution from 6p orbital of Pb-atoms. In the case of NCQDs adsorption, a combined contribution from 2p orbitals of C and N-atoms are found in the bandgap regime of $CsPbBr_3$. These states are predicted to significantly impact carrier mobilities and photo-induced carriers of $CsPbBr_3$ perovskite materials.

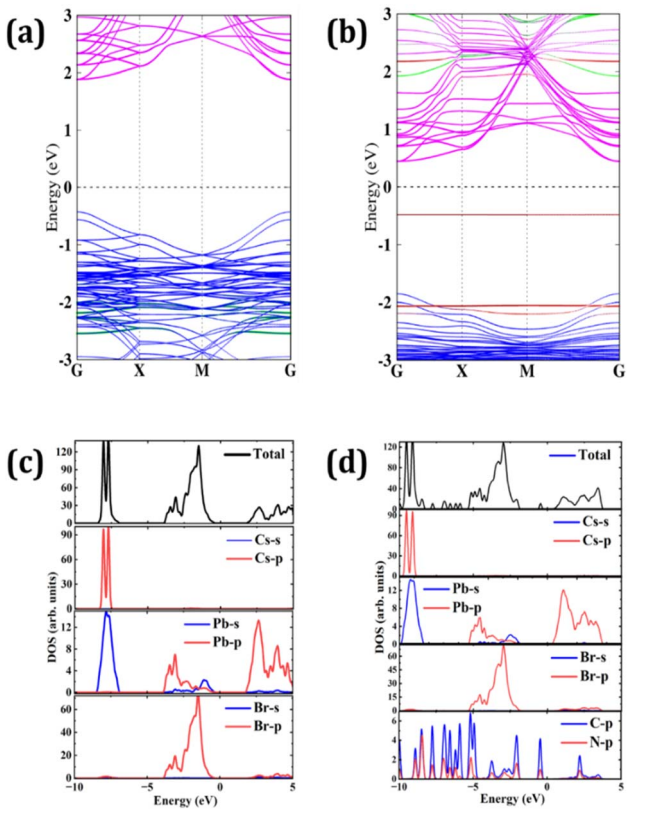

Fig. 8 Projected band structures of (a) $CsPbBr_3$ slab and (b) NCQDs adsorbed on $CsPbBr_3$. Slab (Cs: green, Pb: magenta, Br: blue, C: black, and N: red). Total DOS and PDOS of (c) $CsPbBr_3$ slab and (d) NCQDs adsorbed on $CsPbBr_3$. Fermi level is set at 0 eV.

Conclusions

In conclusion, we synthesized $CsPbBr_3$ NCs with different shelling materials by LARP synthesis process and synthesized NCQDs *via* hydrothermal process. We characterized the $CsPbBr_3$ NCs, NCQDs, and their heterostructures by various characterization techniques. The PL intensity of the $CsPbBr_3$ NCs quenches with successive addition of NCQDs. The rate of PL quenching of the NCs is faster when the shell thickness of the NCs is thin and *vice versa*. This result also supported by TRPL measurements where the PL lifetime value decreases rapidly for thinner shelled NCs. The Stern–Volmer plot affirms that both static and dynamic quenching possesses in the heterostructure. The DFT analysis reflects that NCQDs and $CsPbBr_3$ NCs form a quasi-type II heterostructure with staggered band alignment. The faster charge transfer in thinner-shelled perovskite NCs and NCQDs can be attributed to the bonding between the N-state of NCQDs and the Pb-atoms within the $CsPbBr_3$ structure. The optimized formulation shows better charge transfer properties which are reduced by introducing thicker shelling layers. When NCQDs adsorbed on the Pb–Br terminated surface (100) lattice planes of $CsPbBr_3$ crystal, both the 2p orbitals of C- and N-atoms contribute to the bandgap region of $CsPbBr_3$. These states are expected to strongly influence the mobility of carriers and the generation of photo-induced carriers in $CsPbBr_3$. The study holds significant importance as it offers a valuable understanding of the design and application of different heterostructures, which can be extrapolated to a broad range of applications such as solar cells, LEDs, photodetectors, CO_2 reduction, and photocatalytic activity.

Author contributions

S. B. conceived the research idea and planned the experiments accordingly. S. R. performed the synthesis, characterization, and related experiments. M. R. S. executed the theoretical studies. S. M. helped in TCSPC experiment. The first draft of the manuscript was written by S. R. and S. B. All authors have given approval to the final version of the manuscript. S. B. lead the project.

Conflicts of interest

There are no conflicts to declare.

Acknowledgements

S. B. acknowledges to the Department of Science and Technology (DST), India (Award number# DST/INSPIRE/04/2017/000530) for financial research support. S. R. thanks to ICT-IOC Bhubaneswar for her fellowship.

Notes and references

1 M. V. Kovalenko, L. Protesescu and M. I. Bodnarchuk, Properties and potential optoelectronic applications of lead halide perovskite nanocrystals, *Science*, 2017, **358**, 745–750.

2 Q. A. Akkerman, G. Rainò, M. V. Kovalenko and L. Manna, Genesis, challenges and opportunities for colloidal lead halide perovskite nanocrystals, *Nat. Mater.*, 2018, **17**, 394–405.

3 S. Yakunin, L. Protesescu, F. Krieg, M. I. Bodnarchuk, G. Nedelcu, M. Humer, G. De Luca, M. Fiebig, W. Heiss and M. V. Kovalenko, Low-threshold amplified spontaneous emission and lasing from colloidal nanocrystals of caesium lead halide perovskites, *Nat. Commun.*, 2015, **6**, 8056.

4 A. Swarnkar, A. R. Marshall, E. M. Sanehira, B. D. Chernomordik, D. T. Moore, J. A. Christians, T. Chakrabarti and J. M. Luther, Quantum dot–induced phase stabilization of α-CsPbI3 perovskite for high-efficiency photovoltaics, *Science*, 2016, **354**, 92–95.

5 X.-K. Liu, W. Xu, S. Bai, Y. Jin, J. Wang, R. H. Friend and F. Gao, Metal halide perovskites for light-emitting diodes, *Nat. Mater.*, 2021, **20**, 10–21.

6 Y.-H. Kim, S. Kim, A. Kakekhani, J. Park, J. Park, Y.-H. Lee, H. Xu, S. Nagane, R. B. Wexler, D.-H. Kim, S. H. Jo, L. Martínez-Sarti, P. Tan, A. Sadhanala, G.-S. Park, Y.-W. Kim, B. Hu, H. J. Bolink, S. Yoo, R. H. Friend, A. M. Rappe and T.-W. Lee, Comprehensive defect suppression in perovskite nanocrystals for high-efficiency light-emitting diodes, *Nat. Photonics*, 2021, **15**, 148–155.

7 Y. Zhao and K. Zhu, Organic–inorganic hybrid lead halide perovskites for optoelectronic and electronic applications, *Chem. Soc. Rev.*, 2016, **45**, 655–689.

8 C. C. Stoumpos, C. D. Malliakas, J. A. Peters, Z. Liu, M. Sebastian, J. Im, T. C. Chasapis, A. C. Wibowo, D. Y. Chung, A. J. Freeman, B. W. Wessels and M. G. Kanatzidis, Crystal Growth of the Perovskite Semiconductor CsPbBr3: A New Material for High-Energy Radiation Detection, *Cryst. Growth Des.*, 2013, **13**, 2722–2727.

9 J. Yu, G. Liu, C. Chen, Y. Li, M. Xu, T. Wang, G. Zhao and L. Zhang, Perovskite CsPbBr3 crystals: growth and applications, *J. Mater. Chem. C*, 2020, **8**, 6326–6341.

10 J. Song, Q. Cui, J. Li, J. Xu, Y. Wang, L. Xu, J. Xue, Y. Dong, T. Tian, H. Sun and H. Zeng, Ultralarge All-Inorganic Perovskite Bulk Single Crystal for High-Performance Visible–Infrared Dual-Modal Photodetectors, *Adv. Opt. Mater.*, 2017, **5**, 1700157.

11 L. Protesescu, S. Yakunin, M. I. Bodnarchuk, F. Krieg, R. Caputo, C. H. Hendon, R. X. Yang, A. Walsh and M. V. Kovalenko, Nanocrystals of Cesium Lead Halide Perovskites (CsPbX3, X = Cl, Br, and I): Novel Optoelectronic Materials Showing Bright Emission with Wide Color Gamut, *Nano Lett.*, 2015, **15**, 3692–3696.

12 X. Zhang, X. Bai, H. Wu, X. Zhang, C. Sun, Y. Zhang, W. Zhang, W. Zheng, W. W. Yu and A. L. Rogach, Water-Assisted Size and Shape Control of CsPbBr3 Perovskite Nanocrystals, *Angew. Chem.*, 2018, **57**, 3337–3342.

13 Y. Li, X. Zhang, H. Huang, S. V. Kershaw and A. L. Rogach, Advances in metal halide perovskite nanocrystals: Synthetic strategies, growth mechanisms, and optoelectronic applications, *Mater. Today*, 2020, **32**, 204–221.

14 A. Pan, B. He, X. Fan, Z. Liu, J. J. Urban, A. P. Alivisatos, L. He and Y. Liu, Insight into the Ligand-Mediated Synthesis of Colloidal CsPbBr3 Perovskite Nanocrystals: The Role of Organic Acid, Base, and Cesium Precursors, *ACS Nano*, 2016, **10**, 7943–7954.

15 J. De Roo, M. Ibáñez, P. Geiregat, G. Nedelcu, W. Walravens, J. Maes, J. C. Martins, I. Van Driessche, M. V. Kovalenko and Z. Hens, Highly Dynamic Ligand Binding and Light Absorption Coefficient of Cesium Lead Bromide Perovskite Nanocrystals, *ACS Nano*, 2016, **10**, 2071–2081.

16 S. Bhaumik, S. A. Veldhuis, Y. F. Ng, M. Li, S. K. Muduli, T. C. Sum, B. Damodaran, S. Mhaisalkar and N. Mathews, Highly stable, luminescent core–shell type methylammonium–octylammonium lead bromide layered perovskite nanoparticles, *Chem. Commun.*, 2016, **52**, 7118–7121.

17 G. H. Ahmed, J. Yin, O. M. Bakr and O. F. Mohammed, Successes and Challenges of Core/Shell Lead Halide Perovskite Nanocrystals, *ACS Energy Lett.*, 2021, **6**, 1340–1357.

18 C.-H. Lu, G. V. Biesold-McGee, Y. Liu, Z. Kang and Z. Lin, Doping and ion substitution in colloidal metal halide perovskite nanocrystals, *Chem. Soc. Rev.*, 2020, **49**, 4953–5007.

19 Y. Wang, J. Ren, X. Zhou and G. Zhang, Stability improvements of metal halide perovskite nanocrystals and their optoelectrical applications, *Mater. Chem. Front.*, 2023, **7**, 2175–2207.

20 M. R. Kar, S. Ray, B. K. Patra and S. Bhaumik, State of the art and prospects of metal halide perovskite core@shell nanocrystals and nanocomposites, *Mater. Today Chem.*, 2021, **20**, 100424.

21 D. Yang and D. Huo, Cation doping and strain engineering of CsPbBr3-based perovskite light emitting diodes, *J. Mater. Chem. C*, 2020, **8**, 6640–6653.

22 S. Ray, A. Mohapatra and S. Bhaumik, Synthesis of highly stable double-coated Zn-doped cesium lead bromide nanocrystals for indium ion detection in water, *Mater. Adv.*, 2022, **3**, 4684–4692.

23 A. Mohapatra, S. Kumar, T. K. Acharya, C. Goswami and S. Bhaumik, Highly stable multi-encapsulated red-emitting cesium lead halide nanocrystals for efficient copper ion detection and imaging in live cells, *J. Alloys Compd.*, 2023, **947**, 169453.

24 Y. Duan, C. Ezquerro, E. Serrano, E. Lalinde, J. García-Martínez, J. R. Berenguer and R. D. Costa, Meeting High

Stability and Efficiency in Hybrid Light-Emitting Diodes Based on SiO2/ZrO2 Coated CsPbBr3 Perovskite Nanocrystals, *Adv. Funct. Mater.*, 2020, **30**, 2005401.

25 H. Li, X. Wang, X. Zhu, X. Duan and A. Pan, Composition modulation in one-dimensional and two-dimensional chalcogenide semiconductor nanostructures, *Chem. Soc. Rev.*, 2018, **47**, 7504–7521.

26 Y. Wang, Q. Wang, X. Zhan, F. Wang, M. Safdar and J. He, Visible light driven type II heterostructures and their enhanced photocatalysis properties: a review, *Nanoscale*, 2013, **5**, 8326–8339.

27 S. V. Kershaw, A. S. Susha and A. L. Rogach, Narrow bandgap colloidal metal chalcogenide quantum dots: synthetic methods, heterostructures, assemblies, electronic and infrared optical properties, *Chem. Soc. Rev.*, 2013, **42**, 3033–3087.

28 V. K. Ravi, S. Saikia, S. Yadav, V. V. Nawale and A. Nag, CsPbBr3/ZnS Core/Shell Type Nanocrystals for Enhancing Luminescence Lifetime and Water Stability, *ACS Energy Lett.*, 2020, **5**, 1794–1796.

29 X. Zhang, X. Wu, X. Liu, G. Chen, Y. Wang, J. Bao, X. Xu, X. Liu, Q. Zhang, K. Yu, W. Wei, J. Liu, J. Xu, H. Jiang, P. Wang and X. Wang, Heterostructural CsPbX3-PbS (X = Cl, Br, I) Quantum Dots with Tunable Vis–NIR Dual Emission, *J. Am. Chem. Soc.*, 2020, **142**, 4464–4471.

30 A. Kipkorir, J. DuBose, J. Cho and P. V. Kamat, CsPbBr3–CdS heterostructure: stabilizing perovskite nanocrystals for photocatalysis, *Chem. Sci.*, 2021, **12**, 14815–14825.

31 G. Yin, X. Qi, Y. Chen, Q. Peng, X. Jiang, Q. Wang, W. Zhang and X. Gong, Constructing an all zero-dimensional CsPbBr3/CdSe heterojunction for highly efficient photocatalytic CO2 reduction, *J. Mater. Chem. A*, 2022, **10**, 22468–22476.

32 X. Wang, J. He, L. Mao, X. Cai, C. Sun and M. Zhu, CsPbBr3 perovskite nanocrystals anchoring on monolayer MoS2 nanosheets for efficient photocatalytic CO2 reduction, *Chem. Eng. J.*, 2021, **416**, 128077.

33 S. Zhang, R. Guo, H. Zeng, Y. Zhao, X. Liu, S. You, M. Li, L. Luo, M. Lira-Cantu, L. Li, F. Liu, X. Zheng, G. Liao and X. Li, Improved performance and stability of perovskite solar modules by interface modulating with graphene oxide crosslinked CsPbBr3 quantum dots, *Energy Environ. Sci.*, 2022, **15**, 244–253.

34 T. Chen, G. Tong, E. Xu, H. Li, P. Li, Z. Zhu, J. Tang, Y. Qi and Y. Jiang, Accelerating hole extraction by inserting 2D Ti3C2-MXene interlayer to all inorganic perovskite solar cells with long-term stability, *J. Mater. Chem. A*, 2019, **7**, 20597–20603.

35 X. Song, X. Liu, D. Yu, C. Huo, J. Ji, X. Li, S. Zhang, Y. Zou, G. Zhu, Y. Wang, M. Wu, A. Xie and H. Zeng, Boosting Two-Dimensional MoS2/CsPbBr3 Photodetectors via Enhanced Light Absorbance and Interfacial Carrier Separation, *ACS Appl. Mater. Interfaces*, 2018, **10**, 2801–2809.

36 E. Rathore, K. Maji, D. Rao, B. Saha and K. Biswas, Charge Transfer in the Heterostructure of CsPbBr3 Nanocrystals with Nitrogen-Doped Carbon Dots, *J. Phys. Chem. Lett.*, 2020, **11**, 8002–8007.

37 M. R. Kar, U. Patel and S. Bhaumik, Highly stable and water dispersible polymer-coated CsPbBr 3 nanocrystals for Cu-ion detection in water, *Mater. Adv.*, 2022, **3**, 8629–8638.

38 M. R. Kar, R. Chakraborty, U. Patel, R. Chakraborty, S. Ray, T. K. Acharya, C. Goswami and S. Bhaumik, Impact of Zn-doping on the composition, stability, luminescence properties of silica coated all-inorganic cesium lead bromide nanocrystals and their biocompatibility, *Mater. Today Chem.*, 2022, **23**, 100753.

39 A. Tan, G. Yang and X. Wan, Ultra-high quantum yield nitrogen-doped carbon quantum dots and their versatile application in fluorescence sensing, bioimaging and anti-counterfeiting, *Spectrochim. Acta, Part A*, 2021, **253**, 119583.

40 G. Kresse and J. Furthmüller, Efficiency of ab-initio total energy calculations for metals and semiconductors using a plane-wave basis set, *Comput. Mater. Sci.*, 1996, **6**, 15–50.

41 G. Kresse and J. Furthmüller, Efficient iterative schemes for ab initio total-energy calculations using a plane-wave basis set, *Phys. Rev. B*, 1996, **54**, 11169–11186.

42 J. P. Perdew, K. Burke and M. Ernzerhof, Generalized Gradient Approximation Made Simple, *Phys. Rev. Lett.*, 1996, **77**, 3865–3868.

43 S. Grimme, Semiempirical GGA-type density functional constructed with a long-range dispersion correction, *J. Comput. Chem.*, 2006, **27**, 1787–1799.

44 J. Ye, M. M. Byranvand, C. O. Martínez, R. L. Z. Hoye, M. Saliba and L. Polavarapu, Defect passivation in lead-halide perovskite nanocrystals and thin films: toward efficient LEDs and solar cells, *Angew. Chem.*, 2021, **133**, 21804–21828.

45 X. Wu, M. T. Trinh, D. Niesner, H. Zhu, Z. Norman, J. S. Owen, O. Yaffe, B. J. Kudisch and X. Y. Zhu, Trap States in Lead Iodide Perovskites, *J. Am. Chem. Soc.*, 2015, **137**, 2089–2096.

46 Q. Zhong, M. Cao, H. Hu, D. Yang, M. Chen, P. Li, L. Wu and Q. Zhang, One-Pot Synthesis of Highly Stable CsPbBr3@SiO2 Core–Shell Nanoparticles, *ACS Nano*, 2018, **12**, 8579–8587.

47 V. Naresh and N. Lee, Zn(II)-Doped Cesium Lead Halide Perovskite Nanocrystals with High Quantum Yield and Wide Color Tunability for Color-Conversion Light-Emitting Displays, *ACS Appl. Nano Mater.*, 2020, **3**, 7621–7632.

48 S. Bhaumik, Oriented Attachment of Perovskite Cesium Lead Bromide Nanocrystals, *ChemistrySelect*, 2019, **4**, 4538–4543.

49 J. T. DuBose, A. Christy, J. Chakkamalayath and P. V. Kamat, Transformation of Perovskite Nanoplatelets to Large Nanostructures Driven by Solvent Polarity, *ACS Mater. Lett.*, 2022, **4**, 93–101.

50 X. Hu, Y. Xu, J. Wang, J. Ma, L. Wang and W. Jiang, Ligand-modified synthesis of shape-controllable and highly luminescent CsPbBr3 perovskite nanocrystals under ambient conditions, *Inorg. Chem. Front.*, 2022, **9**, 6080–6090.

51 M. R. Kar, S. Kumar, T. K. Acharya, C. Goswami and S. Bhaumik, Highly water-stable, luminescent, and monodisperse polymer-coated CsPbBr3 nanocrystals for imaging in living cells with better sensitivity, *RSC Adv.*, 2023, **13**, 5946–5956.

52 A. Mohapatra, M. R. Kar and S. Bhaumik, Suppression of halide migration and improved stability in double-coated cesium lead halide perovskite nanocrystals for application in down-conversion white-light-emitting diodes, *J. Alloys Compd.*, 2022, **927**, 166972.
53 H. Zhang, X. Wang, Q. Liao, Z. Xu, H. Li, L. Zheng and H. Fu, Embedding Perovskite Nanocrystals into a Polymer Matrix for Tunable Luminescence Probes in Cell Imaging, *Adv. Funct. Mater.*, 2017, **27**, 1604382.
54 Y. Liu, F. Li, L. Qiu, K. Yang, Q. Li, X. Zheng, H. Hu, T. Guo, C. Wu and T. W. Kim, Fluorescent Microarrays of in Situ Crystallized Perovskite Nanocomposites Fabricated for Patterned Applications by Using Inkjet Printing, *ACS Nano*, 2019, **13**, 2042–2049.
55 F. Gao, W. Yang, X. Liu, Y. Li, W. Liu, H. Xu and Y. Liu, Highly stable and luminescent silica-coated perovskite quantum dots at nanoscale-particle level via nonpolar solvent synthesis, *Chem. Eng. J.*, 2021, **407**, 128001.
56 H. Ding, S.-B. Yu, J.-S. Wei and H.-M. Xiong, Full-Color Light-Emitting Carbon Dots with a Surface-State-Controlled Luminescence Mechanism, *ACS Nano*, 2016, **10**, 484–491.
57 Y. Choi, B. Kang, J. Lee, S. Kim, G. T. Kim, H. Kang, B. R. Lee, H. Kim, S.-H. Shim, G. Lee, O.-H. Kwon and B.-S. Kim, Integrative Approach toward Uncovering the Origin of Photoluminescence in Dual Heteroatom-Doped Carbon Nanodots, *Chem. Mater.*, 2016, **28**, 6840–6847.
58 D. Chen, W. Wu, Y. Yuan, Y. Zhou, Z. Wan and P. Huang, Intense multi-state visible absorption and full-color luminescence of nitrogen-doped carbon quantum dots for blue-light-excitable solid-state-lighting, *J. Mater. Chem. C*, 2016, **4**, 9027–9035.
59 K. Jiang, Y. Wang, X. Gao, C. Cai and H. Lin, Facile, Quick, and Gram-Scale Synthesis of Ultralong-Lifetime Room-Temperature-Phosphorescent Carbon Dots by Microwave Irradiation, *Angew. Chem., Int. Ed.*, 2018, **57**, 6216–6220.
60 D. Chao, W. Lyu, Y. Liu, L. Zhou, Q. Zhang, R. Deng and H. Zhang, Solvent-dependent carbon dots and their applications in the detection of water in organic solvents, *J. Mater. Chem. C*, 2018, **6**, 7527–7532.
61 S. Bhaumik, A. Bruno and S. Mhaisalkar, Broadband emission from zero-dimensional Cs4PbI6 perovskite nanocrystals, *RSC Adv.*, 2020, **10**, 13431–13436.
62 J. Byun, H. Cho, C. Wolf, M. Jang, A. Sadhanala, R. H. Friend, H. Yang and T.-W. Lee, Efficient Visible Quasi-2D Perovskite Light-Emitting Diodes, *Nat. Commun.*, 2016, **28**, 7515–7520.
63 A. Sharma and J. Das, Small molecules derived carbon dots: synthesis and applications in sensing, catalysis, imaging, and biomedicine, *J. Nanobiotechnol.*, 2019, **17**, 92.
64 S. Muduli, P. Pandey, G. Devatha, R. Babar, M. Thripuranthaka, D. C. Kothari, M. Kabir, P. P. Pillai and S. Ogale, Photoluminescence Quenching in Self-Assembled CsPbBr3 Quantum Dots on Few-Layer Black Phosphorus Sheets, *Angew. Chem., Int. Ed.*, 2018, **57**, 7682–7686.
65 Y. Dong, H. Pang, H. B. Yang, C. Guo, J. Shao, Y. Chi, C. M. Li and T. Yu, Carbon-Based Dots Co-doped with Nitrogen and Sulfur for High Quantum Yield and Excitation-Independent Emission, *Angew. Chem., Int. Ed.*, 2013, **52**, 7800–7804.
66 G. Chen, J. Seo, C. Yang and P. N. Prasad, Nanochemistry and nanomaterials for photovoltaics, *Chem. Soc. Rev.*, 2013, **42**, 8304–8338.
67 L. Mishra, R. K. Behera, A. Panigrahi and M. K. Sarangi, Förster Resonance Energy Transfer Assisted Enhancement in Optoelectronic Properties of Metal Halide Perovskite Nanocrystals, *J. Phys. Chem. Lett.*, 2022, **13**, 4357–4364.
68 Y. Yuan, R. Xu, H.-T. Xu, F. Hong, F. Xu and L.-J. Wang, Nature of the band gap of halide perovskites ABX3 (A = CH3NH3, Cs; B = Sn, Pb; X = Cl, Br, I): First-principles calculations, *Chin. Phys. B*, 2015, **24**, 116302.
69 H. M. Ghaithan, Z. A. Alahmed, S. M. H. Qaid, M. Hezam and A. S. Aldwayyan, Density Functional Study of Cubic, Tetragonal, and Orthorhombic CsPbBr3 Perovskite, *ACS Omega*, 2020, **5**, 7468–7480.